Light Load Efficiency Improvement of DAB Converters With Optimal Switching Sequences

Ziheng Xiao, *Member, IEEE*, Muxuan Xiao, Zhixing He, *Member, IEEE*, Liang Wang, Zongjian Li, *Member, IEEE*, and Hongliang Wang, *Senior Member, IEEE*

***Abstract*—This article introduces a method to enhance the light load efficiency of dual active bridge converters through power loss minimization via optimal switching sequences. Peak efficiency points for various operational conditions are identified using a comprehensive power loss calculation approach. Single phase shift modulation and trapezoidal current modulation modes are utilized, and an iterative algorithm determines the optimal switching sequence for the first, repeating, and final switching pulses under a given peak inductor current in various operating condition. The comprehensive state machine diagram of the proposed control method demonstrates seamless integration of both continuous and burst modes for efficiency improvement. Experimental waveforms, efficiency curves, and power loss breakdown diagrams from a 1 kW prototype demonstrate that the proposed method significantly outperforms continuous operation mode, as well as conventional and advanced burst modes, increasing light load efficiency from below 60% to above 85%.**

***Index Terms*—Burst mode, dual active bridge converter, light-load efficiency improvement.**

I. Introduction

With development of power electronic conversion applications such as dc data centers [1], [2], consumer electronics [3], [4], energy storage systems [5], [6], [7], and electric vehicles [8], [9] has been explosive. This has resulted in a higher demand for efficiency in power conversion circuits, not just at heavy loads but also at light loads. In some typical applications, such as 80 Plus [10] and Energy Star [11], high efficiency is required even at loads below 10%.

The dual active bridge (DAB) converter is expected to play an important role in bidirectional power transmission applications as it can operate in both buck and boost modes with superior transient response and high efficiency [12]. Numerous modulation schemes and control methods have been proposed to improve the efficiency of DAB in different operating conditions. Doncker et al. [13] proposed the original and simplest single phase shift (SPS) modulation scheme, which showed high efficiency in heavy load conditions. However, when the DAB output-to-input voltage ratio deviates from unity in light load conditions, the power switches lose their zero voltage switching-ON (ZVS-ON) ability. Additionally, both the root mean square (rms) value and the peak value of the inductor current ($I_{\rm rms}$ and $I_{\rm Peak}$) increase. To address this issue, dual phase shift and extended phase shift modulation schemes were proposed in [14], [15], [16], and [17] to eliminate reactive power and extend the ZVS-ON regions in some operating points. The triple phase shift discussed in [18] and [19] provides three degrees of freedom to reduce the power loss of a DAB with a wide operating range. The triangular current modulation (TCM) and trapezoidal current modulation (TRM) proposed in [20] aim to reduce the conduction and copper losses in low and medium power conditions.

In light load conditions, achieving ZVS-ON of all power switches is not easy, resulting in predominant switching losses. Choi et al. [21] and Everts et al. [22] proposed the All-ZVS modulation scheme that enables ZVS-ON of all power switches at the cost of increased conduction loss. Oggier and Ordonez [23] and Hiltunen et al. [24] used varying switching frequency to extend the ZVS-ON region of DAB. Riedel et al. [25], Qin et al. [26], and Liu and Duan [27] used modified circuit topologies to maintain the ZVS-ON regions of DAB. Recently, some artificial intelligence based methods [28], [29], [30] are utilized for DAB efficiency improvement.

Despite the various modulation schemes and methods discussed above, the efficiency of DAB still remains inadequate when the load drops to 10% or lower. In addition to the continuous operating methods, the burst mode is an effective way to improve the light load efficiency by switching the converter between ON and OFF modes. During the burst-ON time, $T_{\rm ON}$, the DAB operates with peak efficiency, and the output voltage increases. During the burst-OFF time, $T_{\rm OFF}$, all the power switches are turned OFF and the output voltage decreases. Generally, burst mode has the potential to boost the light load efficiency of converters close to peak efficiency [31], [32], [33]. However, controlling the converter can be challenging due to the dynamics and oscillations at the boundary of the burst-ON/burst-OFF modes. In [31], hysteresis burst mode with a predefined hysteresis band

Received 5 August 2024; revised 29 September 2024 and 11 November 2024; accepted 4 December 2024. Date of publication 9 December 2024; date of current version 14 April 2025. This work was supported by the National Natural Science Foundation of China under Grant 52177180 and Grant 52125705. Recommended for publication by Associate Editor A. Safaee. *(Corresponding author: Muxuan Xiao.)*

Ziheng Xiao is with the College of Electrical and Information Engineering, Hunan University, Changsha 410082, China, and also with the Energy Research Institute, Nanyang Technological University, Singapore 639798 (e-mail: zihengxiao@hnu.edu.cn).

Muxuan Xiao, Zhixing He, Liang Wang, Zongjian Li, and Hongliang Wang are with the College of Electrical and Information Engineering, Hunan University, Changsha 410082, China (e-mail: xiaomuxuan@hnu.edu.cn; hezhixing@hnu.edu.cn; wangl@cseco.cn; lzjq1@hnu.edu.cn; wanghl123@hnu.edu.cn).

Color versions of one or more figures in this article are available at https://doi.org/10.1109/TPEL.2024.3513412.

Digital Object Identifier 10.1109/TPEL.2024.3513412

is used. The design of the hysteresis band is critical, as a larger band can induce a large output voltage ripple, while a small band leads to low efficiency. In [32] and [33], constant burst frequency control and constant T_{ON} control are proposed to reduce audible noise and output voltage ripple.

State trajectory analysis has been used to explain the operation of converters in burst mode. Feng et al. [34] proposed optimal trajectory control and its simplified version to improve the efficiency of *LLC* converters. The first switching pulse is also optimized in [35]. Based on this work, Fei et al. [36] proposed three, five, and seven switching sequences that were implemented using a digital signal processor.

In summary, burst mode control provides an effective way to boost converter efficiency in light load conditions. Some of the previous articles analyzed the performance of the converter under different burst mode controls, while others focused on digital implementation and optimization in typical operating points. However, there is a need for a generic and quantitative method to select the optimal switching sequence for DAB in burst mode.

To address this missing gap, this article investigates the optimal burst mode operation switching sequence for improving light load efficiency. First, it presents the power loss calculations for burst mode under varying voltage gains, output power, and peak inductor current conditions. Based on these calculations, the optimal switching sequence, including the first, repeating, and final pulses, is analyzed. A detailed state machine diagram illustrates the proposed method, which selects the optimal switching sequence for different conditions, ensuring a smooth and seamless transition within the burst mode and between burst mode to continuous operation mode.

Experimental results compare the proposed method with continuous operation modes, as well as conventional and advanced burst mode control methods. The efficiency curves and detailed power loss breakdown diagrams show that continuous operation modes suffer from high-frequency hard-switching (HS) or high conduction loss. Conventional and advanced burst mode control methods lack switching sequence optimization, leading to suboptimal efficiency. In contrast, the proposed method optimizes the switching sequence for power loss minimization, increasing light load efficiency from below 60% to above 85%.

The contributions of this article include the following.

1) Derivation of a power loss minimization-oriented burst mode optimal switching sequence for flexible light load efficiency improvement.
2) An iterative algorithm for determining switching sequences for the first, repeating, and final pulses in burst mode for practical implementation.
3) A comprehensive state machine diagram for the control algorithm of the DAB converter, enabling flexible and efficient operation in both continuous and burst modes.

The rest of this article is organized as follows. Section II analyzes the power loss breakdown of a DAB under multiple modulation schemes and discusses the operation characteristics of burst mode. Section III presents the operation stage equations and optimal switching sequences for SPS and TRM

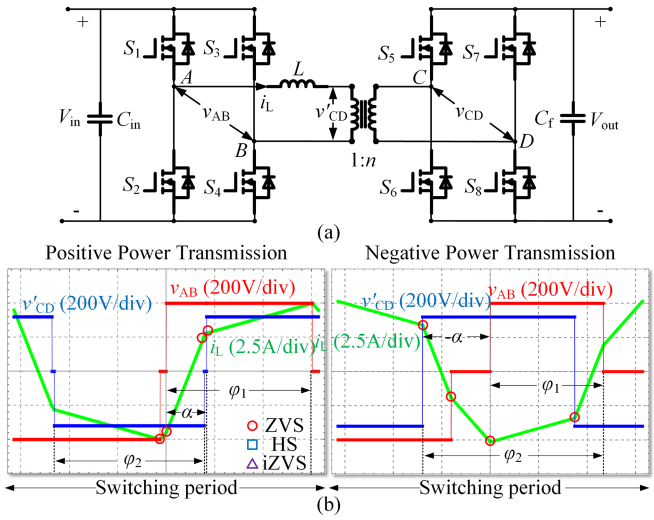

Fig. 1. (a) Topology diagram of DAB. (b) Typical waveforms of DAB with positive/negative power transmission.

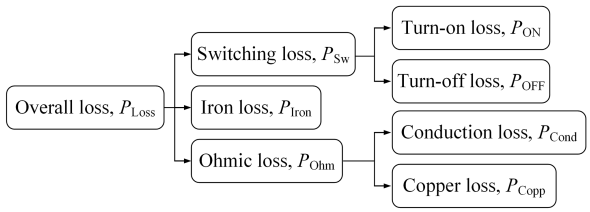

Fig. 2. Classification and definition of the overall power loss of DAB.

modes. Section IV discusses the experimental results. Finally, Section V concludes this article.

II. Power Loss Under Different Modulation Schemes

The topology diagram of the DAB is depicted in Fig. 1(a). C_{in} and C_f are the input and output dc capacitors. S_1–S_8 are 8 power MOSFETs. L denotes the power transmission inductor. The turns ratio of the transformer is 1:n. The input and output voltages are V_{in} and V_{out}, while the primary and secondary port voltages of the transformer are v_{AB} and v_{CD}. The reflected value of v_{CD} is v'_{CD}. The inductor current is i_L and the switching frequency is as f_s. As depicted in Fig. 1(b), the power transmission in a DAB can be positive or negative by manipulating the switching sequences of the MOSFETs. Duty ratios in primary bridge φ_1, in secondary bridge φ_2, and the phase shift angle α between two bridges are expressed in radian, respectively. The control parameter of DAB is denoted as (α, φ_1, φ_2). Fig. 1(b) also indicates the ZVS-ON, HS, and incomplete ZVS (iZVS) states of MOSFETs. Due to the symmetric nature of the DAB, this article considers only the operating condition with buck mode and positive power transmission.

A. Power Loss Analysis of DAB

As shown in Fig. 2, the overall power loss of DAB P_{Loss}, can be classified into switching loss P_{SW}, iron loss P_{Iron}, and ohmic loss P_{Ohm} [37]. P_{SW} is further divided into turn-ON

loss, P_{ON}, and turn-OFF loss. P_{OFF}. P_{Ohm} is further divided into conduction loss P_{Cond} and copper loss P_{Copp}. During the deadtime when both MOSFETs in one leg are turned OFF, the energy stored in the inductor must be greater than the energy exchanged by the two nonlinear MOSFET parasitic capacitors C_{oss} [38]. Assuming the inductor current I_{d} is reduced to zero at the end of the switching process, the minimum ZVS boundary inductor current $I_{\mathrm{d\text{-}min}}$ is given as

$$\frac{LI_{\mathrm{d}}^2}{2} \geq Q_{\mathrm{oss}}\left(V_{\mathrm{in}}\right) V_{\mathrm{in}} \Rightarrow I_{\mathrm{d-min}} = \sqrt{\frac{2Q_{\mathrm{oss}}\left(V_{\mathrm{in}}\right) V_{\mathrm{in}}}{L}} \tag{1}$$

where $Q_{\mathrm{oss}}(v)$ is the voltage-dependent charge of the nonlinear MOSFET parasitic capacitors.

When (1) is satisfied, $P_{\mathrm{ON}} = E_{\mathrm{ON}} \times f_{\mathrm{s}}$ is negligible. Otherwise, there will be residual drain-source voltage ΔV on the C_{oss}. This part of energy is also dissipated in the MOSFET. The expression of E_{ON} in the iZVS condition is given as

$$\begin{aligned} E_{\mathrm{ON}} = {} & E_{\mathrm{oss}}\left(\Delta V\right) + V_{\mathrm{in}}\left(Q_{\mathrm{oss}}\left(V_{\mathrm{in}}\right) - Q_{\mathrm{oss}}\left(V_{\mathrm{in}} - \Delta V\right)\right) \\ & - \left(E_{\mathrm{oss}}\left(V_{\mathrm{in}}\right) - E_{\mathrm{oss}}\left(V_{\mathrm{in}} - \Delta V\right)\right) \end{aligned} \tag{2}$$

where $E_{\mathrm{oss}}(v)$ is the voltage-dependent energy stored in the nonlinear capacitance.

Assuming a constant inductor current during the deadtime t_{d}, the expression of ΔV can be roughly derived as

$$\Delta V = V_{\mathrm{in}} - \frac{V_{\mathrm{in}}}{I_{\mathrm{d}}} t_{\mathrm{d}}. \tag{3}$$

The turn-OFF loss, $P_{\mathrm{OFF}} = E_{\mathrm{OFF}} \times f_{\mathrm{s}}$, is formed by the instantaneous current and voltage of C_{oss}. The turn-OFF energy loss E_{OFF} of a power switch with turn-OFF current I_{SW} is expressed as

$$E_{\mathrm{OFF}} = \int_0^{T_{\mathrm{f}}} I_{\mathrm{SW}} v_{\mathrm{ds}} dt = \frac{T_{\mathrm{f}}^2 I_{\mathrm{SW}}^2}{48 C_{\mathrm{oss}}} \tag{4}$$

where v_{ds} is the drain-source voltage of the MOSFET, and T_{f} is the time it takes for the current to fall linearly from I_{SW} to $I_{\mathrm{SW}}/2$.

P_{Iron} is divided into the iron loss of the inductor $P_{\mathrm{Iron\text{-}L}}$ and the iron loss of the transformer $P_{\mathrm{Iron\text{-}T}}$. As for $P_{\mathrm{Iron\text{-}L}}$, considering the nonsinusoidal waveform of the flux density, we use the improved generalized Steinmetz equation to calculate core loss [39]. This method assumes that instantaneous core losses are a function of B and its rate of change

$$P_{\mathrm{Iron-L}} = V_{\mathrm{e}} \times \frac{1}{T_{\mathrm{s}}} \int_0^{T_{\mathrm{s}}} k_{\mathrm{i}} \left| \frac{\mathrm{d}B\left(t\right)}{\mathrm{d}t} \right|^{\alpha} \left(2B_{\mathrm{ac}}\right)^{\beta-\alpha} \mathrm{d}t \tag{5}$$

$$k_{\mathrm{i}} = \frac{k}{\left(2\pi\right)^{\alpha-1} \int_0^{2\pi} \left|\cos\left(\theta\right)\right|^{\alpha} 2^{\beta-\alpha} \mathrm{d}\theta} \approx \frac{k}{2^{\beta-1}\pi^{\alpha-1}\left(0.28 + \frac{1.7}{\alpha+1.4}\right)} \tag{6}$$

where k, α, and β are the Steinmetz coefficients of the material, and V_{e} is the effective volume of the core. $P_{\mathrm{Iron\text{-}T}}$ can be calculated similarly.

Round Litz wires are used as the windings for the inductors. Copper losses caused by the skin effect and proximity effect are calculated using modified Bessel functions. The skin effect and proximity effect losses, denoted as P_{Skin} and P_{Prox}, can be simplified as

$$P_{\mathrm{Skin}} \approx \frac{2}{\pi\sigma d_{\mathrm{r}}^2} i_{\mathrm{Lac}}^2, P_{\mathrm{Prox}} \approx \frac{\pi\sigma^2 f_{\mathrm{s}}^2 d_{\mathrm{r}}^2}{32} i_{\mathrm{Lac}}^2 \tag{7}$$

where σ is the material conductivity and d_{r} is the diameter of the Litz wires [28].

The conduction loss P_{Cond} can be calculated by summing all the resistive components, which is proportional to the square of I_{rms}, which can be expressed as

$$P_{\mathrm{Cond}} = \left(r_{\mathrm{eq1}} + r_{\mathrm{eq2}}\right) I_{\mathrm{rms}}^2 \tag{8}$$

where r_{eq1} is the equivalent resistance of the power MOSFETs, and r_{eq2} is the equivalent resistance of the primary/secondary windings and the power inductor.

By combining (1)–(8), the analytical expression for P_{Loss} can be derived. The efficiency, η, can be calculated as

$$\eta = \frac{P_{\mathrm{o}}}{P_{\mathrm{o}} + P_{\mathrm{Loss}}}. \tag{9}$$

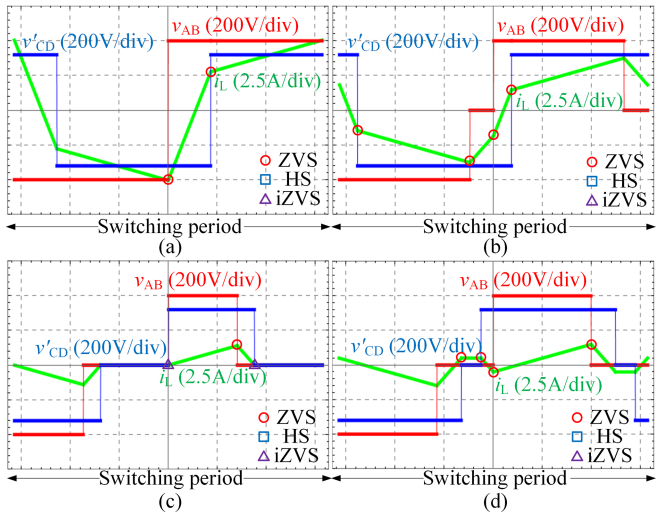

Fig. 3. Typical waveforms of DAB with different modulation schemes. (a) SPS. (b) TRM. (c) TCM. (d) All-ZVS.

B. Efficiency Curves Under Different Modulation Schemes

We calculated the efficiency curves of the DAB under four modulation schemes: SPS, TRM, TCM, and All-ZVS, based on (9). The typical normalized waveforms for these modulation schemes with $M = 0.8$ are shown in Fig. 3. A comparison of these modulation schemes is presented in Table I.

SPS and TRM are preferred for high and medium power conditions. According to [18] and [19], the control parameters and corresponding peak inductor current I_{Peak} for SPS and TRM are given from

$$\alpha = \frac{\left(1 - \sqrt{1-P}\right)\pi}{2}, \varphi_1 = \pi, \varphi_2 = \pi \tag{10a}$$

$$I_{\mathrm{Peak}} = \begin{cases} \frac{\pi}{2}\left(1 - M\sqrt{1-P}\right) \wedge M \in (0,1) \\ \frac{\pi}{2}\left(M - \sqrt{1-P}\right) \wedge M \in [1,\infty) \end{cases} \tag{10b}$$

TABLE I
COMPARISON OF DIFFERENT MODULATION SCHEMES

Modulation schemes	Features
SPS	High efficiency when $M \approx 1$. ZVS-on is not achieved when M deviates from unity or in low power conditions, leading to high P_{SW}, P_{Iron}, and P_{Ohm}.
TRM	Achieves minimum P_{Ohm} in medium power conditions; ZVS-on is possible when M deviates from unity.
TCM	Achieves minimum P_{Ohm} in low power conditions with iZVS.
All-ZVS	Achieves minimum P_{SW} in low power conditions at the cost of increased P_{Ohm}.

$$\alpha = \frac{1}{2}\left(1 - \sqrt{\frac{1-P}{M^2+(M-1)^2}}\right)\pi \tag{11a}$$

$$\varphi_1 = \left(1-(1-M)\sqrt{\frac{1-P}{M^2+(M-1)^2}}\right)\pi, \varphi_2 = \pi \tag{11b}$$

$$I_{\text{Peak}} = \frac{\pi}{2}\left(\pi - \sqrt{(1-P)\left(M^2+(M-1)^2\right)}\right)$$

$$\forall P \in [2M(1-M),1] \wedge M \in (0,1) \tag{11c}$$

$$\alpha = \frac{1}{2}\left(1+(M-2)\sqrt{\frac{1-P}{(M-1)^2+1}}\right)\pi \tag{12a}$$

$$\varphi_1 = \pi, \varphi_2 = \left(1-(1-M)\sqrt{\frac{1-P}{(M-1)^2+1}}\right)\pi \tag{12b}$$

$$I_{\text{Peak}} = \frac{\pi}{2}\left(M - \sqrt{(1-P)\left((M-1)^2+1\right)}\right)$$

$$\forall P \in \left[\frac{2(M-1)}{M^2},1\right] \wedge M \in \left[1,\infty\right) \tag{12c}$$

where P is normalized output power, and the base value P_{Base} is given as

$$P_{\text{Base}} = \frac{nV_{\text{in}}V_{\text{out}}}{8f_sL}. \tag{13}$$

In high power conditions, SPS and TRM are suitable due to their relatively low P_{SW}, P_{Iron}, and P_{Ohm}. In comparison, the All-ZVS modulation scheme is more efficient than TCM in low power conditions, as P_{SW} is a major contributor. Each modulation scheme has its advantages and disadvantages. The efficiency curves for these schemes in this typical DAB converter are depicted in Fig. 4, with the electric parameters summarized in Table II.

Based on the calculated P_{Loss}, the peak efficiency curve and corresponding output power are shown in Fig. 5. The red and blue lines indicate peak efficiency achieved via SPS and TRM, respectively. Note the mode change point at $M = 0.67$, with a boundary efficiency of 97.2% and corresponding output power

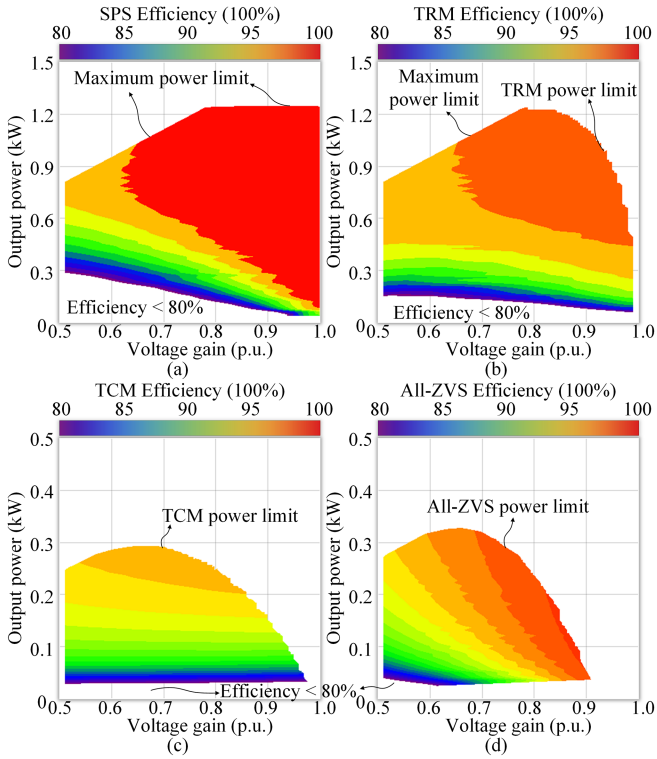

Fig. 4. Calculated efficiency of DAB with different modulation schemes. (a) SPS. (b) TRM. (c) TCM. (d) All-ZVS.

TABLE II
THE ELECTRIC PARAMETERS OF THE DAB CONVERTER

Variable	Value
Input voltage (V)	500
Output voltage (V)	300–400
Turn ratio	1:1
Power inductor (μH)	200
Switching frequency (kHz)	50
Power inductor core parameters and core loss calculation coefficients	Magnetics high flux 060 core, core volume V_{eL} = 21 300 mm^3, k = 47.51, α = 1.585, β = 1.43. (Frequency in kHz, and flux density in T).
Transformer core parameters and core loss calculation coefficients	N95 material, core volume V_{eT} = 34 120 mm^3, k = 6.91E-8, α= 1.5294, β = 2.8505. (Frequency in kHz, and flux density in mT).

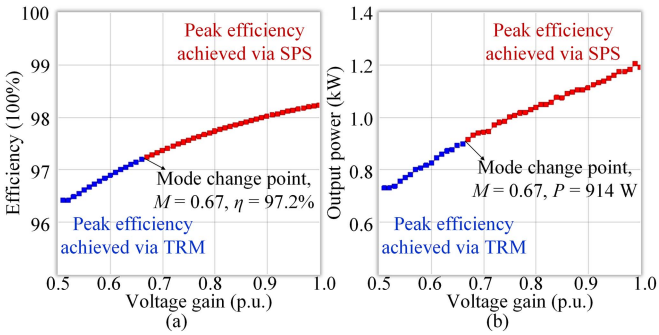

Fig. 5. (a) Peak efficiencies of DAB achieved via SPS and TRM in different voltage gain conditions. (b) Corresponding output power with peak efficiencies in different voltage gain conditions.

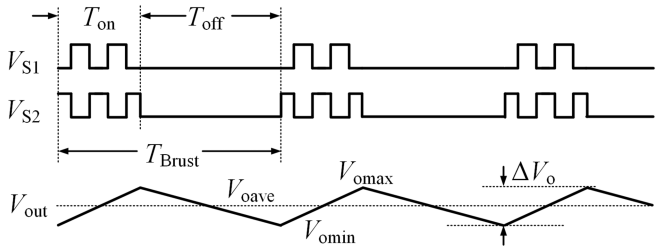

Fig. 6. Diagram of the burst mode in DAB.

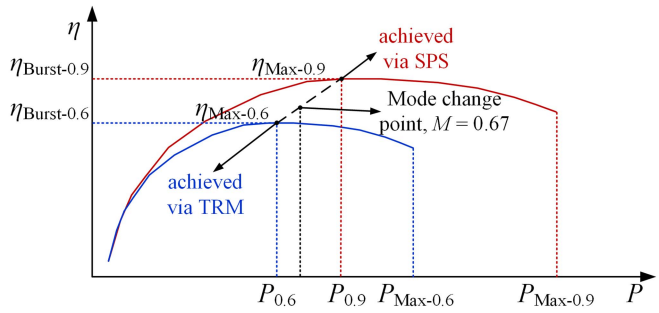

Fig. 7. Typical efficiency curves of DAB in burst mode.

of 914 W. For $M > 0.67$, SPS shows higher efficiency, while for $M < 0.67$, TRM is more efficient.

C. Operation Characteristic of Burst Mode in DAB

As depicted in Fig. 6, burst mode periodically blocks the switch-gate driving signals V_{S1} and V_{S2} to reduce the power loss (illustrated for S_1 and S_2). The burst period T_{Burst} and burst duty ratio D_{Burst} are defined as

$$T_{\mathrm{Burst}} = T_{\mathrm{on}} + T_{\mathrm{off}}, D_{\mathrm{Burst}} = \frac{T_{\mathrm{on}}}{T_{\mathrm{on}} + T_{\mathrm{off}}}. \tag{14}$$

During T_{ON}, the gate signals are activated. The input and output energies of DAB are denoted as $E_{\mathrm{in\text{-}ON}}$, and $E_{\mathrm{o\text{-}ON}}$, which can be expressed as

$$E_{\mathrm{in-on}} = P_{\mathrm{in}} T_{\mathrm{on}}, E_{\mathrm{o-on}} = P_{\mathrm{o}} T_{\mathrm{on}},$$
$$E_{\mathrm{in-on}} - E_{\mathrm{o-on}} = \frac{C_{\mathrm{f}} V_{\mathrm{omax}}^2}{2} - \frac{C_{\mathrm{f}} V_{\mathrm{omin}}^2}{2} = C_{\mathrm{f}} V_{\mathrm{oave}} \Delta V_{\mathrm{o}} \tag{15}$$

where P_{in} and P_{o} denote the input and output power of DAB. V_{omax} and V_{omin} denote the maximum and minimum output voltage, V_{oave} and ΔV_{o} denote the average output voltage and voltage ripple.

During T_{OFF}, the power balance equations are

$$E_{\mathrm{in-off}} = 0, E_{\mathrm{o-off}} = P_{\mathrm{o}} T_{\mathrm{off}}$$
$$E_{\mathrm{in-off}} - E_{\mathrm{o-off}} = \frac{C_{\mathrm{f}} V_{\mathrm{omin}}^2}{2} - \frac{C_{\mathrm{f}} V_{\mathrm{omax}}^2}{2} = -C_{\mathrm{f}} V_{\mathrm{oave}} \Delta V_{\mathrm{o}}. \tag{16}$$

In one burst period, the output voltage returns to the steady-state value, where

$$P_{\mathrm{in}} T_{\mathrm{on}} = P_{\mathrm{o}} T_{\mathrm{off}} + P_{\mathrm{o}} T_{\mathrm{on}} \Rightarrow P_{\mathrm{in}} D_{\mathrm{Burst}} = P_{\mathrm{o}}. \tag{17}$$

The output voltage ripple ΔV_{o} is given as

$$\Delta V_{\mathrm{o}} = \frac{P_{\mathrm{o}} (1 - D_{\mathrm{Burst}}) T_{\mathrm{Burst}}}{C_{\mathrm{f}} V_{\mathrm{oave}}} = \frac{P_{\mathrm{o}} (P_{\mathrm{in}} - P_{\mathrm{o}}) T_{\mathrm{Burst}}}{C_{\mathrm{f}} V_{\mathrm{oave}} P_{\mathrm{in}}}. \tag{18}$$

When properly controlled in burst mode, the initial inductor current in T_{OFF} is zero, making P_{SW}, P_{Iron}, and P_{Ohm} zero. Because there is no power loss during T_{OFF}, the efficiency of DAB in burst mode equals the efficiency during T_{ON}.

The efficiency curves of DAB in continuous operation mode are depicted in Fig. 7. The red and blue lines represent the efficiency curves for $M = 0.9$ and $M = 0.6$, respectively. The maximum efficiencies ($\eta_{\mathrm{Max\text{-}0.9}}$ and $\eta_{\mathrm{Max\text{-}0.6}}$) are achieved via SPS and TRM with $P_{0.9}$ and $P_{0.6}$ power transmission. Denote the theoretical efficiency of burst mode when $M = 0.9$ as $\eta_{\mathrm{Burst\text{-}0.9}}$, we can achieve $\eta_{\mathrm{Burst\text{-}0.9}} = \eta_{\mathrm{Max\text{-}0.9}}$ via SPS in the burst-ON time. D_{Burst} and T_{Burst} are adjusted by the load condition and ΔV_{o}, respectively.

III. Optimal Switching Sequences in Burst Mode

In burst mode, DAB is more susceptible to current asymmetry and spikes due to the absence of dc blocking capacitors between the inverter bridges and the transformer. This section focuses on determining the optimal switching sequences in burst mode to mitigate dc current bias, implement ZVS, and improve efficiency within a predefined peak current limit.

A. Operation Stage Equations in Burst Mode

As depicted in Fig. 8, there are 7 equivalent stages of DAB considering a resistive load R_{L} in burst mode (the reflected value of V_{o} is denoted as V'_{o}). The equivalent circuits for these stages can be derived as follows. For example, applying Kirchhoff's voltage and current laws to stage 1 yields

$$\begin{cases} i_1(t) = i_{10} + \frac{(V_{\mathrm{in}} + V'_{\mathrm{o1}}(t))t}{L} \\ V'_{\mathrm{o1}}(t) = V'_{\mathrm{o1}} - \frac{(i_1(t) + I_{\mathrm{o}}(t))t}{n^2 C_{\mathrm{f}}} \\ I_{\mathrm{o}}(t) = \frac{nV'_{\mathrm{o1}}(t)}{R_{\mathrm{L}}} \end{cases} \tag{19}$$

where $i_1(t)$ and $V'_{\mathrm{o1}}(t)$ denote the inductor current and the output voltage, i_{10} and V'_{o1} denote the initial values of $i_1(t)$ and $V'_{\mathrm{o1}}(t)$.

Hence, $V'_{\mathrm{o1}}(t)$ and $i_1(t)$ can be solved as

$$\begin{cases} V'_{\mathrm{o1}}(t) = \frac{n^2 C_{\mathrm{f}} L R_{\mathrm{L}} V'_{\mathrm{o1}} - R_{\mathrm{L}}(V_{\mathrm{in}} t + i_{10} L) t}{n^2 C_{\mathrm{f}} R_{\mathrm{L}} + (nL + R_{\mathrm{L}} t) t} \\ i_1(t) = \frac{n(nC_{\mathrm{f}} R_{\mathrm{L}} + t)(V_{\mathrm{in}} t + i_{10} L) + n^2 C_{\mathrm{f}} R_{\mathrm{L}} V'_{\mathrm{o1}}}{n^2 C_{\mathrm{f}} R_{\mathrm{L}} + (nL + R_{\mathrm{L}} t) t}. \end{cases} \tag{20}$$

For stages 2–6, similar expressions of $V'_{\mathrm{o2}}(t)$–$V'_{\mathrm{o6}}(t)$ and $i_2(t)$–$i_6(t)$ can be derived. Stage 7 occurs during T_{OFF} where all the power switches are turned-OFF. $V'_{\mathrm{o7}}(t)$ and $i_7(t)$ in stage 7 are given as

$$\begin{cases} V'_{\mathrm{o7}}(t) = \frac{nC_{\mathrm{f}} R_{\mathrm{L}} V'_{\mathrm{o7}}}{nC_{\mathrm{f}} R_{\mathrm{L}} + t} \\ i_7(t) = i_{70}. \end{cases} \tag{21}$$

According to these expressions and the continuity characteristic of i_{L} and V'_{o}, the waveforms of DAB during burst mode can be solved cycle by cycle.

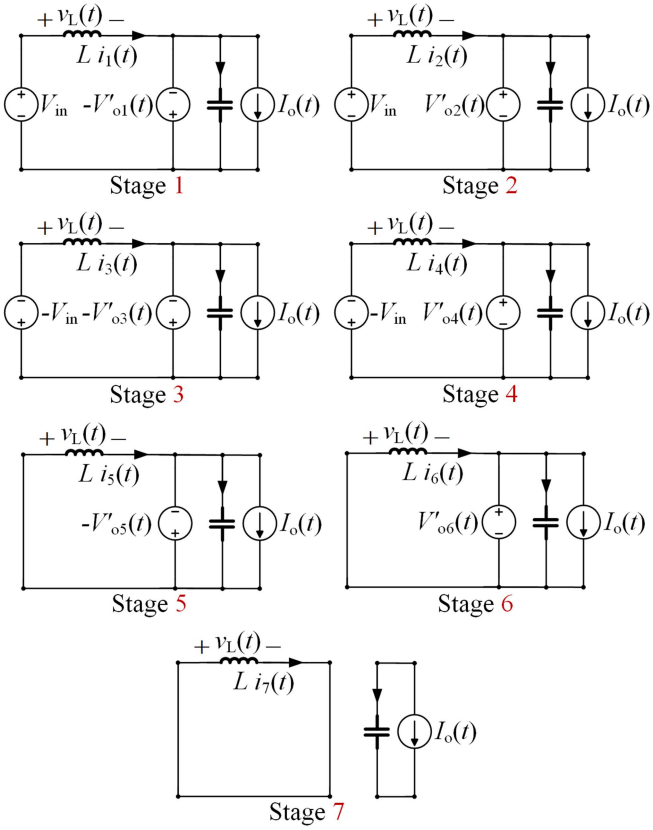

Fig. 8. Seven equivalent stages of DAB in burst mode.

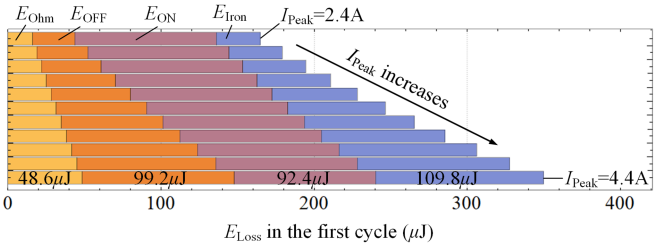

Fig. 9. Energy loss in the first cycle in burst mode.

B. Optimal Switching Sequences in the First Cycle

The burst-OFF time is usually much longer than one switching period. Since all MOSFETs are deactivated, there is no path for the inductor current, and it can be assumed to be zero at the start of the first switching cycle. In the first cycle, both the primary and secondary power switches operate in iZVS. The energy loss in the first cycle is calculated as follows:

$$E_{\text{Loss}} = E_{\text{ON}} + E_{\text{OFF}} + E_{\text{Ohm}} + E_{\text{Iron}} = E_{\text{ON}} + E_{\text{OFF}} + \frac{(r_{\text{eq1}} + r_{\text{eq2}})\, I_{\text{RMS}}^2}{f_{\text{s}}} + \frac{P_{\text{VL}} V_{\text{eL}} + P_{\text{VT}} V_{\text{eT}}}{f_{\text{s}}}. \tag{22}$$

The energy loss composition (in μJ) when I_{Peak} varies from 2.4 to 4.4 A is depicted in Fig. 9. E_{ON} remains constant, while E_{Ohm}, E_{OFF}, and E_{Iron} all increase with higher I_{Peak}.

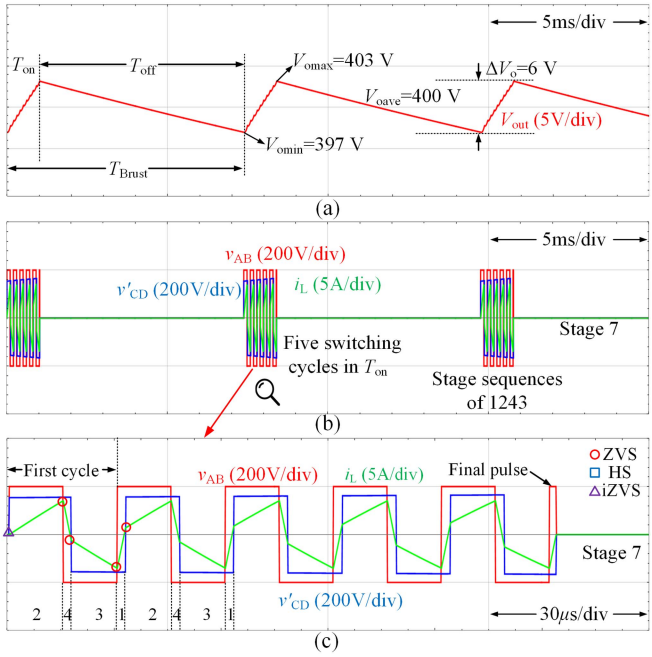

Fig. 10. Typical waveforms of switching sequence "1243" with SPS in burst mode. (a) The output voltage waveform. (b) The waveforms of vAB, v'CD, and iL. (c) The zoomed waveforms of vAB, v'CD, and iL.

After the first cycle, SPS and TRM are the two candidates to be used according to the voltage gain conditions.

C. Optimal Switching Sequences With SPS and TRM

SPS is used when $M > 0.67$. Typical waveforms for $V_{\text{oave}} = 400$ V ($M = 0.8$), $\Delta V_{\text{o}} = 6$ V are depicted in Fig. 10. In this case, there is $I_{\text{Peak}} = 3.5$ A, $T_{\text{Burst}} = 7.36$ ms, $D_{\text{Burst}} = 0.137$. There are five switching cycles during T_{ON}, with the sequence "1243". The zoomed waveforms during T_{on} are illustrated in Fig. 10(c). V_{o} gradually increase in the following four switching cycles. After $V_{\text{o}} > V_{\text{oave}} + \Delta V_{\text{o}}/2$, the last stage sequence ends. Since i_{L} is not returned to zero, there will be voltage and current oscillation if the final pulse is not activated.

During the whole burst period, P_{Loss} is calculated as

$$P_{\text{Loss}} = P_{\text{ON}} + P_{\text{OFF}} + P_{\text{Ohm}} + P_{\text{Iron}} = \sum (E_{\text{ON}} + E_{\text{OFF}}) + \left(\frac{P_{\text{VL}} V_{\text{eL}} + P_{\text{VT}} V_{\text{eT}} + (r_{\text{eq1}} + r_{\text{eq2}})\, I_{\text{RMS}}^2}{f_{\text{s}}} \right) N_{\text{Sw}}. \tag{23}$$

Here, P_{ON} and P_{OFF} are calculated for each switching process, while P_{Ohm} and P_{Iron} are estimated using steady-state values. N_{Sw} indicates the number of switching cycles during T_{ON}.

TRM is more efficient than SPS when $M < 0.67$. Typical waveforms for $V_{\text{oave}} = 300$ V ($M = 0.6$), $\Delta V_{\text{o}} = 4$ V in TRM are depicted in Fig. 11. In this case, there is $I_{\text{Peak}} = 4.5$ A, $T_{\text{Burst}} = 5.16$ ms, $D_{\text{Burst}} = 0.107$. There are three switching cycles with sequence "126435" during T_{ON}. The zoomed waveforms during T_{ON} are illustrated in Fig. 11(c). The method to determine the optimal switching sequences with TRM, as well as the calculation of P_{Loss} can be obtained similarly.

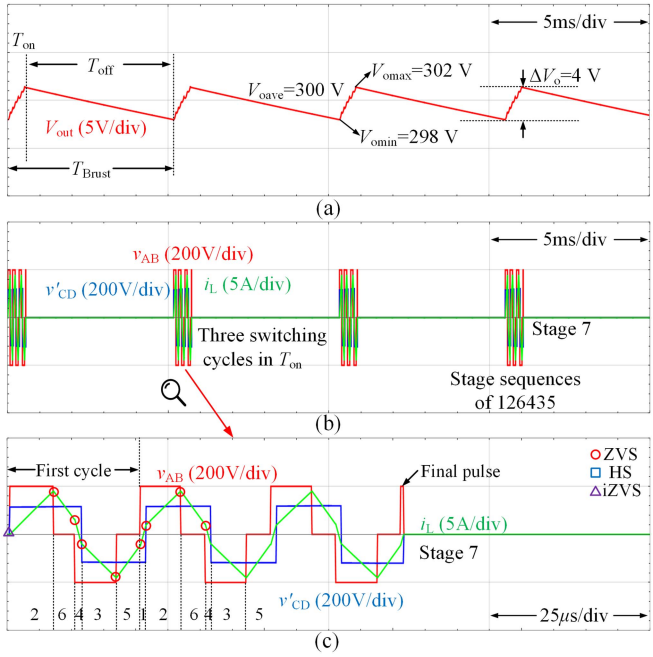

Fig. 11. Typical waveforms of switching sequence "126435" with TRM in burst mode. (a) The output voltage waveform. (b) The waveforms of vAB, v'CD, and iL. (c) The zoomed waveforms of vAB, v'CD, and iL.

The algorithm for determining optimal stage sequences in burst mode is depicted in Fig. 12. The inputs are voltage gain M, the power transmission P, and the peak inductor current I_{Peak}. Based on M, either SPS or TRM is used. In each scenario, the first pulse $\{\alpha(1), \varphi_1(1), \varphi_2(1)\}$, the repeating pulse $\{\alpha(R), \varphi_1(R), \varphi_2(R)\}$, and the final pulse $\{\alpha(F), \varphi_1(F), \varphi_2(F)\}$ are determined. First, initialization sets the initial output voltage V_{Init} as the minimum output voltage V_{omin}, and the initial inductor current I_{Init} as zero. For the first pulse, $\{\alpha(1), \varphi_1(1), \varphi_2(1)\}$ are obtained given M, P, and I_{Peak}, and power loss is calculated $P_{\text{Loss}} = P_{\text{ON}} + P_{\text{OFF}} + P_{\text{Ohm}} + P_{\text{Iron}}$ based on (22). For the repeating sequence, V_{Init} and I_{Init} are derived from V_{End} and I_{End} of the previous cycle. Control parameters are then calculated based on (10)–(12), and operation stage constraints are checked for validity. End values V_{End} and I_{End} are saved as the initial values for the next cycle. This process repeats until V_{End} exceeds V_{omax}. A final pulse ensures I_{End} returns zero to mitigate oscillations at the start of burst-OFF mode.

The algorithm outputs include power losses, efficiency, and optimal switching patterns (the first, repeating, and final pulses). Iteratively running this algorithm provides control parameter relations for different voltage gains, output power, and peak inductor current conditions.

Based on the obtained optimal switching patterns, the delivered energy P_{Del}, can be calculated cycle-by-cycle. Combining P_{Loss} and P_{Del}, the efficiency curves in burst mode with different switching cycles are depicted in Fig. 13. Fig. 13(a) illustrates the delivered energy under different voltage gain conditions. One cycle ($N_{\text{Sw}} = 1$) consists of the first switching pulse, one repeating pulse, and one final switching pulse. Since the power delivered during the first switching pulse is less than that of the

Algorithm: Optimal switching sequences in burst mode

Input: Operation condition: M, P, I_{Peak}.
Initialization: $V_{\text{Init}} \leftarrow V_{\text{omin}}$, $I_{\text{Init}} \leftarrow 0$.
If ($M > 0.67$){
  // SPS mode, calculation of the first cycle (sequence 243):
  $P_{\text{Loss}} = P_{\text{ON}} + P_{\text{OFF}} + P_{\text{Ohm}} + P_{\text{Iron}}$;
  $V_{\text{End}} \leftarrow V'_{o3}(t_3)$, $I_{\text{End}} \leftarrow i_3(t_3)$. //$\{\alpha(1), \varphi_1(1), \varphi_2(1)\}$
  repeat
    $V_{\text{Init}} \leftarrow V_{\text{End}}$, $I_{\text{Init}} \leftarrow I_{\text{End}}$.
    Calculation of control parameter under I_{Peak}
    Check the constraint conditions
    $P_{\text{Loss}} = P_{\text{ON}} + P_{\text{OFF}} + P_{\text{Ohm}} + P_{\text{Iron}}$;
    $V_{\text{End}} \leftarrow V'_{o3}(t_3)$, $I_{\text{End}} \leftarrow i_3(t_3)$.
  until $V_{\text{End}} > V_{\text{omax}}$ //$\{\alpha(R), \varphi_1(R), \varphi_2(R)\}$
  Calculation of the final pulse. //$\{\alpha(F), \varphi_1(F), \varphi_2(F)\}$
}
If ($M < 0.67$){
  // TRM mode, calculation of the first cycle (sequence 24635):
  $P_{\text{Loss}} = P_{\text{ON}} + P_{\text{OFF}} + P_{\text{Ohm}} + P_{\text{Iron}}$;
  $V_{\text{End}} \leftarrow V'_{o5}(t_5)$, $I_{\text{End}} \leftarrow i_5(t_5)$. //$\{\alpha(1), \varphi_1(1), \varphi_2(1)\}$
  repeat
    $V_{\text{Init}} \leftarrow V_{\text{End}}$, $I_{\text{Init}} \leftarrow I_{\text{End}}$.
    Calculation of control parameter under I_{Peak}
    Check the constraint conditions
    $P_{\text{Loss}} = P_{\text{ON}} + P_{\text{OFF}} + P_{\text{Ohm}} + P_{\text{Iron}}$;
    $V_{\text{End}} \leftarrow V'_{o5}(t_5)$, $I_{\text{End}} \leftarrow i_5(t_5)$.
  until $V_{\text{End}} > V_{\text{omax}}$ //$\{\alpha(R), \varphi_1(R), \varphi_2(R)\}$
  Calculation of the final pulse. //$\{\alpha(F), \varphi_1(F), \varphi_2(F)\}$
}
Output: Power loss and efficiency, the optimal switching patterns.
  1: First switching pulse: $\{\alpha(1), \varphi_1(1), \varphi_2(1)\}$
  2: Repeating switching pulses: $\{\alpha(R), \varphi_1(R), \varphi_2(R)\}$
  3: Final switching pulse: $\{\alpha(F), \varphi_1(F), \varphi_2(F)\}$

Fig. 12. Algorithm to determine the optimal stage sequence in burst mode.

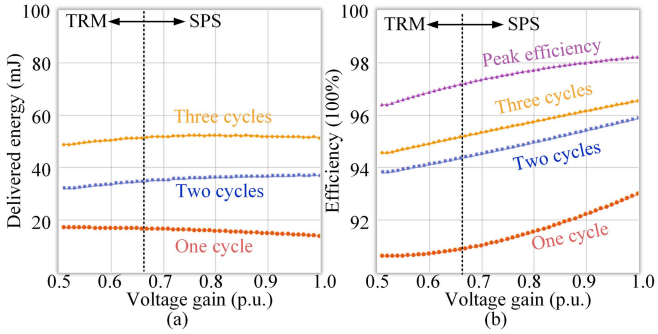

Fig. 13. (a) Calculated efficiency curves of 1–3 switching cycles in different voltage gain conditions. (b) Delivered energy of 1–3 switching cycles in different voltage gain conditions.

repeating pulses, two cycles ($N_{\text{Sw}} = 2$) may not deliver twice the power of one cycle. In Fig. 13(b), the efficiency in one cycle is lower than in multiple cycles for the same reason. The peak efficiency, shown as the purple line, represents the continuous operation efficiency (i.e., $N_{\text{Sw}} >> 1$). In practice, burst mode efficiency is lower than continuous operation efficiency due to additional losses in the first and final switching pulses. As the number of switching cycles increases, the efficiency, delivered energy, and ΔV_{o} all increase.

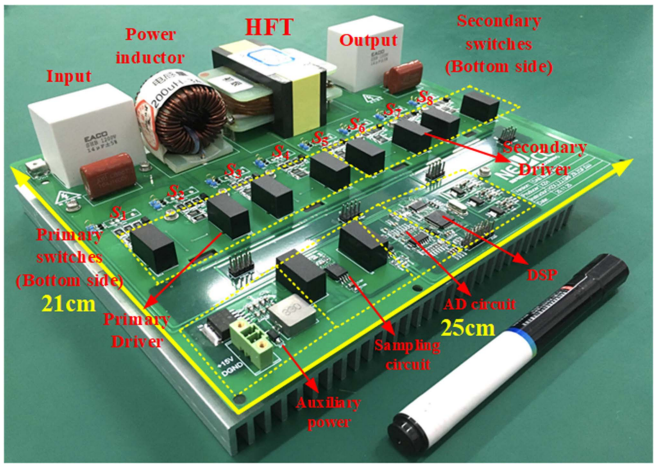

Fig. 14. Experimental platform of the DAB converter prototype.

IV. Experimental Result

The experimental results of different switching sequences in burst mode with a laboratory prototype are depicted in Fig. 14 and the specifications of the experimental prototype are listed below.

1) DC capacitor: 14 μF, 1200 V film capacitor and 10 nF, 1200 V metallized film (CBB) capacitor.
2) Switches: 8 SiC MOSFET C2M0080170P from CREE.
3) Transformer: turn ratio $n = 1{:}1$, EE70, ferrite core.
4) Power transmission inductor: Permalloy core, 200 μH.
5) Input voltage: 500 V, Output voltage: 300 V–400 V.
6) Switching frequency: 50 kHz.
7) Controller: TMS320F28377D C2000 32-bit 200-MHz.

Upon integrating the optimal switching sequences with SPS and TRM, the resulting control scheme is illustrated in the state machine diagram in Fig. 15. This diagram includes four modes: continuous SPS (Mode 1), burst SPS (Mode 2), continuous TRM (Mode 3), and burst TRM (Mode 4), along with their corresponding actions.

Initially, the operation mode is determined based on the sampled values of $V_{\rm in}$, $V_{\rm out}$, $I_{\rm out}$, and the preset values of $I_{\rm Peak}$, $\Delta V_{\rm o}$, $V_{\rm ref}$, $N_{\rm Sw}$, $P_{\rm m}$. Here, $V_{\rm ref}$ is the output voltage reference, $N_{\rm Sw}$ is the preset number of switching cycles in burst mode, and $P_{\rm m}$ is the lower boundary for transitioning from continuous to burst mode. In continuous SPS and TRM mode, a proportional-integral controller regulates the control parameters $(\alpha, \varphi_1, \varphi_2)$, as given in (10)–(12). When the voltage gain exceeds boundary values, the mode switches between continuous SPS and continuous TRM. If the output power falls below $P_{\rm m}$, the converter transitions to the corresponding burst mode.

In burst SPS mode, the optimal switching sequences are activated when $V_{\rm out}$ drops below the lower threshold $V_{\rm ref} - \Delta V_{\rm o}$. Initially, the first pulse $\{\alpha(1), \varphi_1(1), \varphi_2(1)\}$ is applied, and the counter is reset to zero. If the counter is less than $N_{\rm Sw}$, the repeating sequence $\{\alpha(R), \varphi_1(R), \varphi_2(R)\}$ is applied, and the counter increments by one. When the counter reaches $N_{\rm Sw}$, the final pulse $\{\alpha(F), \varphi_1(F), \varphi_2(F)\}$ is enabled, and the counter is reset. The converter then enters the burst-OFF phase, deactivating all MOSFETs until $V_{\rm out}$ drops below the threshold again.

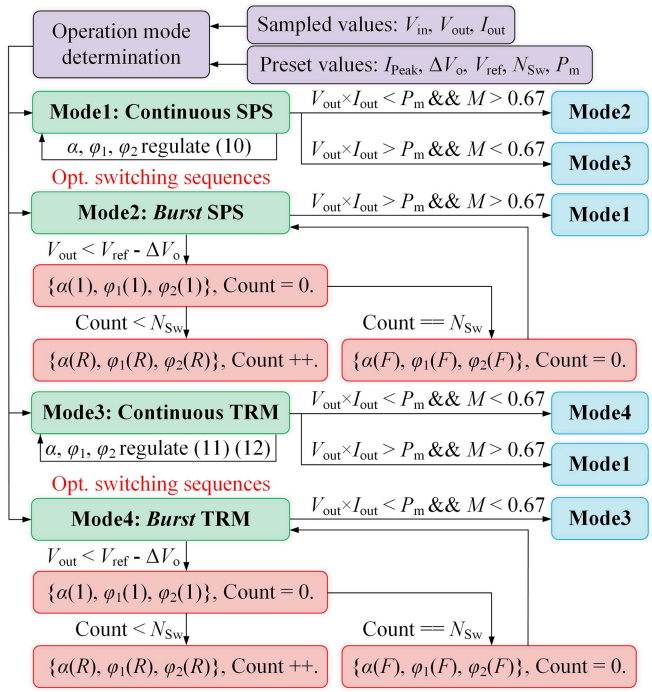

Fig. 15. State machine diagram of the control algorithm for real-time implementation in the DSB converter prototype.

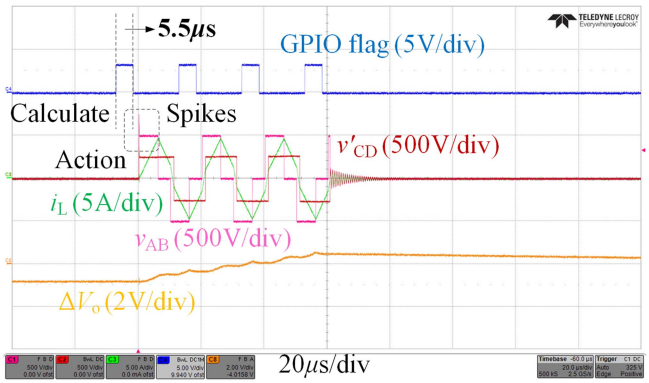

Fig. 16. Execution time of the proposed algorithm.

To test the availability and execution time of the proposed algorithm, we present a typical case in burst TRM mode with the following conditions: $V_{\rm in} = 500$ V, $V_{\rm out} = 250$ V, $I_{\rm Peak} = 5$, $N_{\rm Sw} = 2$, $\Delta V_{\rm o} = 1$ V, and the experimental results is depicted in Fig. 16. We used the general-purpose input/output (GPIO) flag toggles to measure the execution time of the real-time control algorithm, inserted in the ADC interrupt.

When the ADC conversion finishes, the GPIO is set to 3.3 V. All sampled signals at instant k, including $V_{\rm in}[k]$, $V_{\rm out}[k]$, and $I_{\rm out}[k]$, are filtered using a four-bit moving averaging digital filter. Based on the preset values of $I_{\rm Peak}$, $\Delta V_{\rm o}$, $V_{\rm ref}$, $N_{\rm Sw}$, $P_{\rm m}$, and the fitted functions, the control parameters for the first pulse are obtained. The EPWM register values are then calculated and updated, and the GPIO resets to 0 V, sending the PWM signals to the power switches. Since the switching patterns are derived

from $V_{\text{in}}[k]$, $V_{\text{out}}[k]$, and $I_{\text{out}}[k]$, the voltage ripple ΔV_{o} has only a minor influence on the pattern calculations.

The experimental waveform shows the execution time of the proposed method is around 5.5 μs, which is acceptable for a 50 kHz switching frequency (20 μs) DAB converter. All power MOSFETs achieve ZVS, except during the first switching pulse, due to the initial zero inductor current being insufficient to charge or discharge the MOSFET parasitic capacitances. With a rated input voltage of 500 V, voltage spikes on the primary-side MOSFETs reach about 700 V, leaving a safety margin in the selection of SiC MOSFETs for the prototype.

A. Operating Waveforms With Different Modulation Schemes

Steady state waveforms for four operation conditions are shown in Fig. 17: $V_{\text{out}} = 400$ V, $P_{\text{out}} = 1050$ W (with SPS), $V_{\text{out}} = 300$ V, $P_{\text{out}} = 840$ W (with TRM), $V_{\text{out}} = 400$ V, $P_{\text{out}} = 85$ W (with All-ZVS), and $V_{\text{out}} = 300$ V, $P_{\text{out}} = 60$ W (with All-ZVS). ZVS-ON for all power switches is achieved. The efficiencies in SPS and TRM conditions are 97.4% and 96.8%, closely matching the theoretical efficiencies shown in Fig. 5. The corresponding I_{Peak} are 5.1 A, 6.2 A, 2.2 A, and 2.1 A, respectively.

B. Operating Waveforms in Light Load Conditions

We tested two light load conditions: $V_{\text{out}} = 400$ V, $P_{\text{out}} = 85$ W (case 1), and $V_{\text{out}} = 300$ V, $P_{\text{out}} = 60$ W (case 2). In case 1, the waveforms for optimal switching sequences with $N_{\text{Sw}} = 1$ and $N_{\text{Sw}} = 3$ are shown in Fig. 18. Since these is $M = 400/500 = 0.8 > 0.67$, the burst SPS mode is activated. The burst periods T_{Burst} in these two conditions are 177 μs, 624 μs, with corresponding T_{ON} of 19 μs, and 60 μs, respectively. As N_{Sw} increases, T_{Burst}, T_{ON}, and ΔV_{o} all increase, but D_{Burst} remains constant at around 10%. The zoomed waveforms in Fig. 18(b) and (d) show voltage spikes in v_{AB} and v'_{CD} due to iZVS of the power MOSFETs. After the final pulse, i_{L} is nonzero due to parasitic components, causing oscillations at the beginning of T_{OFF}.

For comparison, Fig. 19 shows conventional burst control waveforms with a 1.4 V hysteresis band. During T_{ON}, SPS with $\alpha = 0.1\pi$ is used. There is a dc current bias in i_{L}, risking transformer saturation. The delivered energy per cycle is much smaller than in the optimal switching sequence, resulting in a higher I_{Peak}. Strong oscillations occur during T_{OFF} since the final pulse is not activated.

In case 2, the waveforms for optimal switching sequences with $N_{\text{Sw}} = 1$ and $N_{\text{Sw}} = 3$ are shown in Fig. 20. Since these is $M = 300/500 = 0.6 < 0.67$, the burst TRM mode is activated. The burst periods T_{Burst} in these two conditions are 297 μs, 814 μs, with corresponding T_{ON} of 21 μs, and 63 μs, respectively. Due to lower output power in case 2, T_{Burst} in case 2 is longer than that in case 1.

The light load efficiency improvement method from [23] is also investigated. This method selects burst mode switching sequences based on the natural sequence in half a switching period, then selects the negative counterpart for volt-second

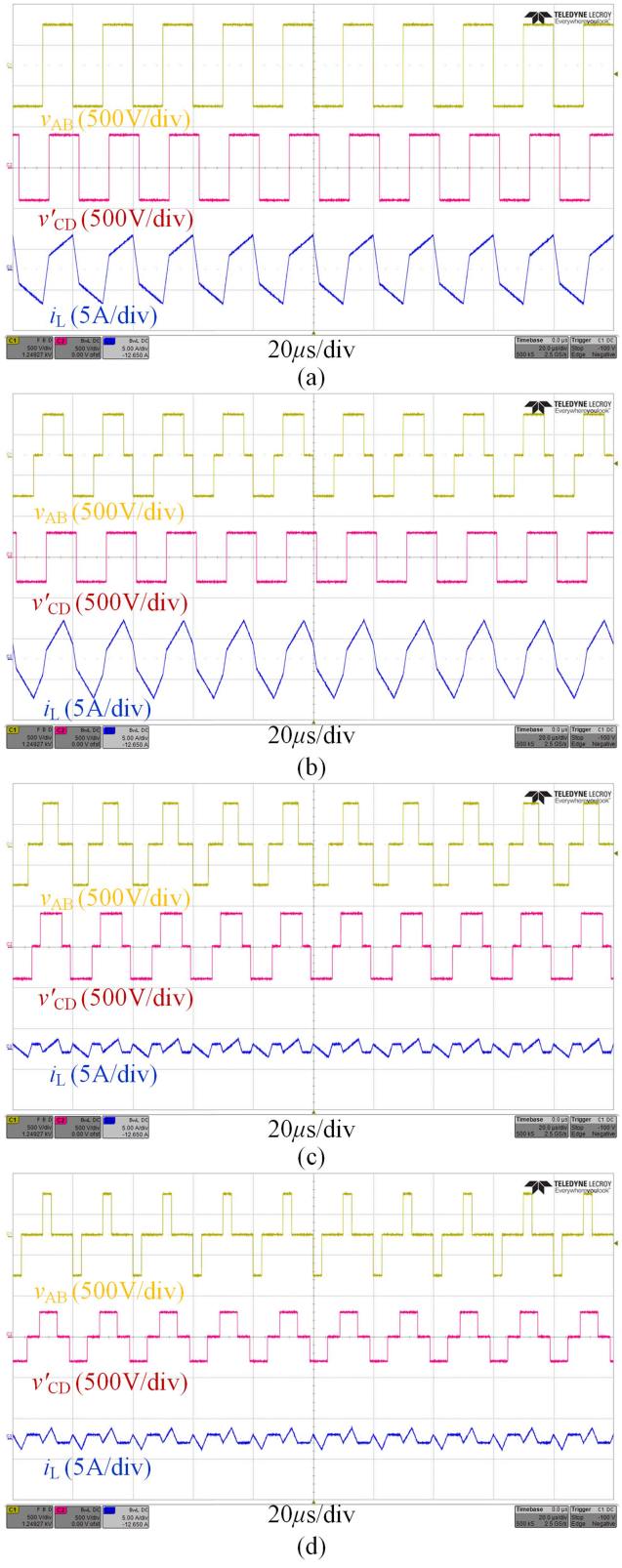

Fig. 17. (a) Steady state waveforms of SPS when $V_{\text{out}} = 400$ V, $P_{\text{out}} = 1050$ W. (b) Steady state waveforms of TRM when $V_{\text{out}} = 300$ V, $P_{\text{out}} = 840$ W. (c) Steady state waveforms of All-ZVS when $V_{\text{out}} = 400$ V, $P_{\text{out}} = 85$ W. (d) Steady state waveforms of All-ZVS when $V_{\text{out}} = 300$ V, $P_{\text{out}} = 60$ W.

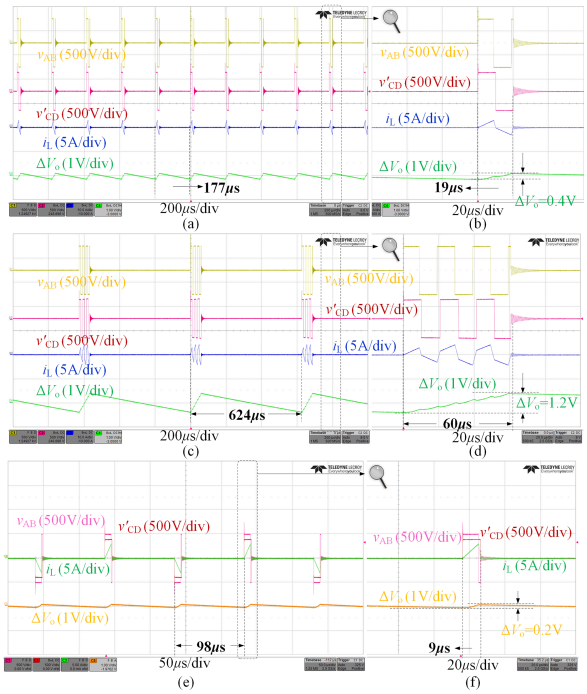

Fig. 18. Waveforms with burst SPS mode in case1. (a) Waveforms with one cycle. (b) Zoomed waveforms with one cycle. (c) Waveforms with three cycles. (d) Zoomed waveforms with three cycles. (e) Burst mode waveforms based on [23]. (f) Zoomed waveforms burst mode waveforms based on [23].

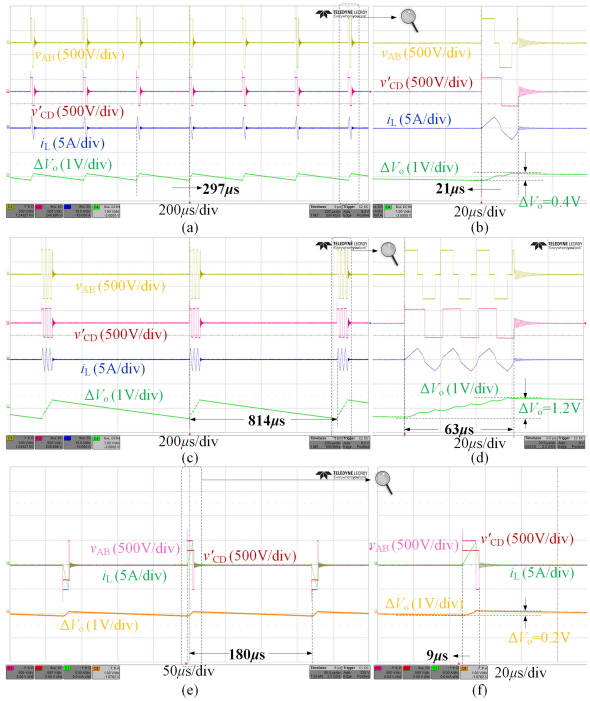

Fig. 20. Waveforms with burst TRM mode in case2. (a) Waveforms with one cycle. (b) Zoomed waveforms with one cycle. (c) Waveforms with three cycles. (d) Zoomed waveforms with three cycles. (e) Burst mode waveforms based on [23]. (f) Zoomed waveforms burst mode waveforms based on [23].

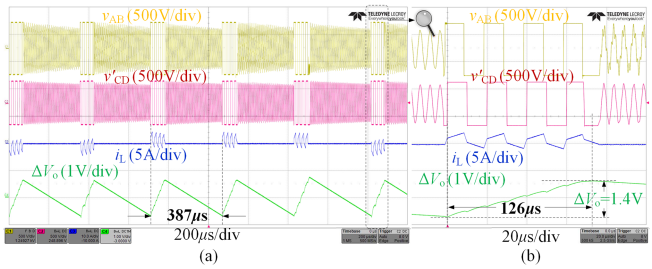

Fig. 19. (a) Typical waveforms of the conventional burst mode control a 1.4 V hysteresis band. (b) Zoomed waveforms during burst-on phase.

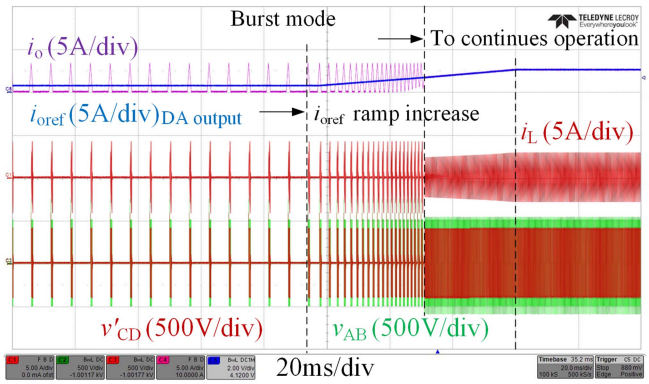

Fig. 21. Dynamic performance of the proposed method with an increase of load. Initially, it employs a fixed three-cycle SPS burst mode. Subsequently, upon the load power escalating to 600 W, it undergoes a seamless transition into continuous SPS mode.

balance. For the given two light load conditions, the waveforms are depicted at the bottom of Figs. 18 and 20. This method is similar to the first switching pulse in the proposed method. Since it uses only one switching cycle, it results in an increased burst frequency. Additionally, due to iZVS in the first switching cycle, increased switching loss occurs. Moreover, as part of the SPS mode, its efficiency decreases with increasing voltage gain mismatch conditions.

We also evaluate the dynamic performance of the proposed method to determine its capability for a seamless transition from burst mode to continuous mode upon an increase in load, as shown in Fig. 21. The burst mode boundary power is set at $P_m = 600$ W. The experimental setup involves connecting the input and output of the prototype to dc voltage sources, with the system operating under output current control mode. The input and output voltages are $V_{in} = 500$ V and $V_{out} = 400$ V. A fixed three-cycle ($N_{Sw} = 3$) burst mode control is deployed, initiating three switching cycles during the burst-ON phase.

The initial output current reference is set at $i_{oref} = 0.7$ A (280 W). At this point, the burst frequency remains constant, and the output current i_o displays a pulse waveform. Subsequently, i_{oref} increases following a predefined slope. As i_{oref} increases, the burst frequency also increases, with the burst mode concluding once i_{oref} reaches approximately 1.5 A. The converter then transitions smoothly to continuous SPS mode as i_{oref} attains 2.5 A. This seamless transition demonstrates that the proposed

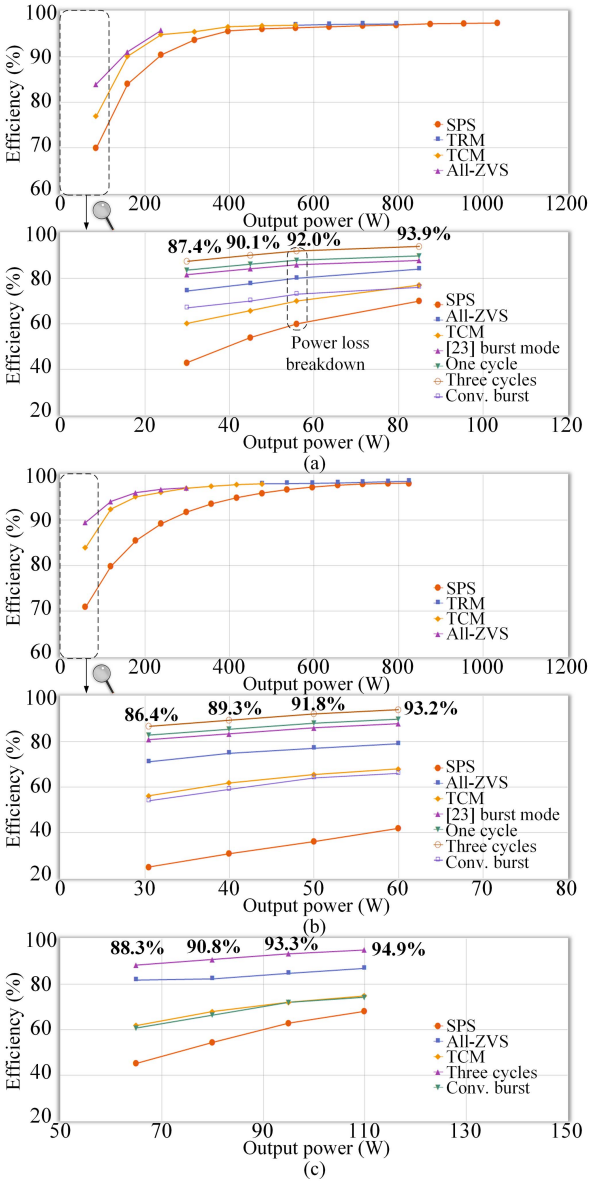

Fig. 22. (a) Efficiency curves when $V_{\text{out}} = 400$ V. (b) Efficiency curves when $V_{\text{out}} = 300$ V. (c) Efficiency curves when $V_{\text{in}} = 750$ V and $V_{\text{out}} = 600$ V. (The power consumption of the sampling, driver, and control circuits are excluded.)

burst mode control can be effectively integrated into the widely used DAB continuous operation mode control strategies.

In summary, the proposed algorithm operates effectively in both continuous operation mode and the proposed burst mode, including steady-state operation and dynamic transitions.

C. Efficiency and Power Loss Breakdown Comparison

The efficiency curves in different operation conditions are depicted in Fig. 22. In case 1, SPS shows the highest efficiency when $P_{\text{o}} > 800$ W, TRM is most efficient for 550 W$< P_{\text{o}} <$ 800 W, and All-ZVS is most efficient when $P_{\text{o}} < 250$ W. The light load efficiency curves at the bottom of Fig. 22(a) show peak efficiencies of 87.4%, 90.1%, 92.0%, and 93.9% with increasing P_{o}. Interestingly, conventional burst control efficiency is lower

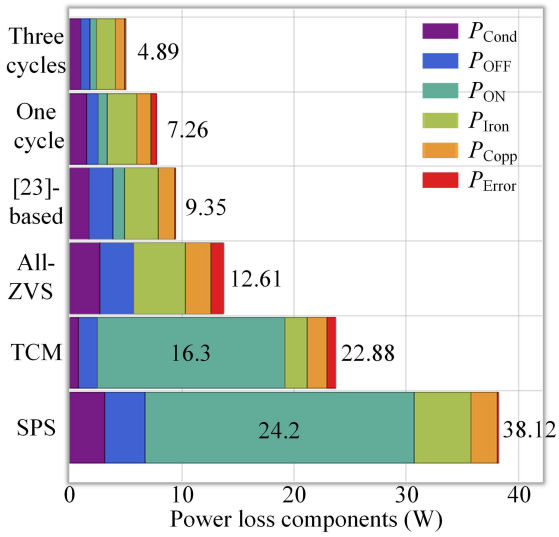

Fig. 23. Detailed power loss breakdown diagram in case 1 with $V_{\text{out}} = 400$ V, and 55 W output power.

than All-ZVS when $P_{\text{o}} < 55$ W. Similar conclusions are drawn in case 2. In Fig. 22(b), peak efficiencies are achieved with All-ZVS, TCM, and TRM as P_{o} increases. SPS efficiency drops rapidly due to high P_{SW} and P_{Ohm}. In light load conditions, peak efficiency is achieved with optimal burst sequences of three switching cycles, despite a larger ΔV_{o}.

With the input voltage increased to 750 V and an output voltage of 600 V, the efficiency curves for different control methods are shown in Fig. 22(c). At around 60 W output power, the SPS mode achieves 45.2% efficiency, significantly lower than the All-ZVS mode at 81.7% and the proposed three-cycle burst mode at 88.3%. At approximately 110 W, the SPS mode reaches 68.1%, and the All-ZVS mode 87.3%, while the proposed three-cycle burst mode attains the highest efficiency at 94.9%. Notably, increasing the input voltage to 750 V enhances efficiency across all operating conditions compared to the 500 V input case.

The measured efficiencies with one and three repeating switching pulses are slightly lower than the calculated values, with less than 5% deviation. This discrepancy is due to oscillations at the burst-ON/burst-OFF boundaries, causing extra losses. Compared to Fig. 19, these oscillations are significantly mitigated with the proposed optimal switching sequences.

The detailed power loss breakdown diagram when $V_{\text{out}} =$ 400 V is depicted in Fig. 23. The power loss components are classified into conduction loss P_{Cond}, turn-OFF loss P_{OFF}, turn-ON loss P_{ON}, iron loss P_{Iron}, and copper loss P_{Copp}, with the difference between calculated and experimental measurements denoted as error power loss P_{Error}. These components are represented by different colors in the diagram.

In SPS and TCM, high-frequency HS results in significant turn-ON losses of 24.2 W and 16.3 W, respectively. High circulating current in SPS also leads to high conduction loss, reducing efficiency to 60% at an output power of 60 W (6% of full load). In contrast, burst mode achieves much higher efficiency, with

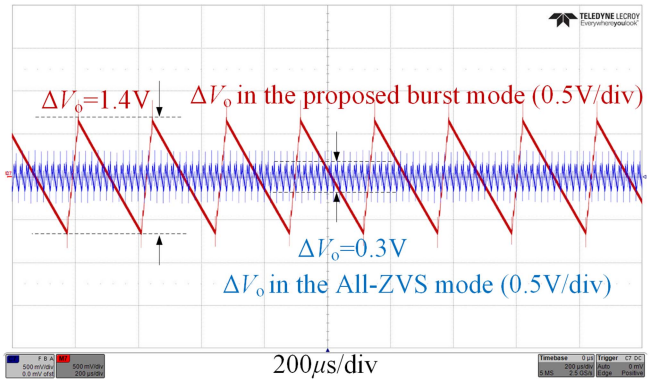

Fig. 24. Output voltage ripple comparison between the continuous All-ZVS mode and the proposed burst mode when $V_{\rm out} = 300$ V, $P_{\rm o} = 60$ W.

TABLE III
COMPARISON OF DIFFERENT LIGHT LOAD EFFICIENCY IMPROVEMENT METHODS

Methods	$T_{\rm Burst}$	$\Delta V_{\rm o}$	Efficiency
TCM [19], [20]*	-	Tiny	Low
All-ZVS [21], [22]*	-	Tiny	Medium
Hysteresis burst	Variable	Medium	Low
Advanced burst mode [23]	Constant	Medium	Medium
[34], [33]†	Constant	Low	Medium
Optimal trajectory [36]†	Variable	Low	High
Proposed method *†	**Variable**	**Adjusted**	**High**

* Burst mode is not applied.
† These methods are only applicable in *LLC* resonant converters.
*† No additional sensors are needed to measure peak current. The control parameters are calculated based on the sampled values of $V_{\rm in}$, $V_{\rm out}$, $I_{\rm out}$, and the preset values of $I_{\rm Peak}$, $\Delta V_{\rm o}$, $V_{\rm ref}$, $N_{\rm Sw}$, $P_{\rm m}$.

total power loss reduced to 9.35 W in the [23]-based burst mode, further reduced to 7.26 W in the proposed one-cycle burst mode, and 4.89 W in the three-cycle burst mode. The calculated power losses match the experimental results within an acceptable error range, verifying the effectiveness of the proposed method.

Table III summarizes the comparison of different light load efficiency improvement methods for DAB. TCM and All-ZVS, being continuous operating methods, maintain a $\Delta V_{\rm o}$ around 0.3 V, significantly smaller than in burst mode (around 0.4 V with one-cycle burst mode and around 1.2 V with three-cycle burst mode). The hysteresis burst mode shows low efficiency due to high $P_{\rm SW}$. Constant $T_{\rm Burst}$ methods, Oggier and Ordonez [23] based advanced burst mode method, and optimal trajectory control methods exhibit relatively high efficiency but are only applicable to *LLC* resonant converters at the resonant frequency, not considering different voltage gain conditions. Conversely, the proposed burst mode control method shows high efficiency, with the output voltage ripple $\Delta V_{\rm o}$ adjustable according to the number of repeating switching pulses during $T_{\rm O\,N}$.

In the final part of this study, we compare the output voltage ripple of continuous operation mode and the proposed burst mode under various conditions. For instance, with a load power of 60 W and an output voltage of 300 V, the output voltage ripple waveforms for continuous All-ZVS mode and the proposed burst mode are measured using a 200 MHz differential voltage probe (HVD3106 from Teledyne LeCroy, 200 MHz bandwidth, ac coupled), as shown in Fig. 24. The results show a ripple voltage of around 300 mV in continuous All-ZVS mode, increasing to 1.4 V in burst mode, which represents only 1.4/300 = 0.47% of the output voltage and is acceptable for practical applications. Although the ripple in the proposed burst mode is significantly higher than that in continuous mode, additional dc link capacitance is unnecessary. Since burst mode is only activated under light load conditions, where load current is minimal, the increased ripple remains manageable.

V. CONCLUSION

This article introduces a method to enhance the light load efficiency of DAB converters by minimizing power loss through optimal switching sequences. Peak efficiency points for various operational conditions are identified using a comprehensive power loss calculation approach. An iterative algorithm determines the optimal switching sequence for the first, repeating, and final pulses under a given peak inductor current condition. The proposed control method demonstrates seamless integration of both continuous and burst modes for improved efficiency. The experimental results from a 1 kW prototype, including waveforms, efficiency curves, and power loss breakdown diagrams, show that the proposed method significantly outperforms continuous operation, as well as conventional and advanced burst modes, increasing light load efficiency from below 60% to above 85%.

APPENDIX

For stages 2–6, $V'_{\rm o2}(t)$–$V'_{\rm o6}(t)$ and $i_2(t)$–$i_6(t)$ are given as

$$\begin{cases} V'_{\rm o2}(t) = \dfrac{n^2C_{\rm f}LR_{\rm L}V'_{\rm o2} - R_{\rm L}(V_{\rm in}t + i_{20}L)t}{n^2C_{\rm f}R_{\rm L} + (nL - R_{\rm L}t)t} \\ i_2(t) = \dfrac{n(nC_{\rm f}R_{\rm L} + t)(V_{\rm in}t + i_{20}L) - n^2C_{\rm f}R_{\rm L}V'_{\rm o2}}{n^2C_{\rm f}R_{\rm L} + (nL - R_{\rm L}t)t} \end{cases} \tag{A1}$$

$$\begin{cases} V'_{\rm o3}(t) = \dfrac{n^2C_{\rm f}LR_{\rm L}V'_{\rm o3} + R_{\rm L}(V_{\rm in}t - i_{30}L)t}{n^2C_{\rm f}R_{\rm L} + (nL + R_{\rm L}t)t} \\ i_3(t) = \dfrac{-n(nC_{\rm f}R_{\rm L} + t)(V_{\rm in}t - i_{30}L) + n^2C_{\rm f}R_{\rm L}V'_{\rm o3}}{n^2C_{\rm f}R_{\rm L} + (nL + R_{\rm L}t)t} \end{cases} \tag{A2}$$

$$\begin{cases} V'_{\rm o4}(t) = \dfrac{n^2C_{\rm f}LR_{\rm L}V'_{\rm o4} + R_{\rm L}(V_{\rm in}t - i_{40}L)t}{n^2C_{\rm f}R_{\rm L} + (nL - R_{\rm L}t)t} \\ i_4(t) = \dfrac{n(nC_{\rm f}R_{\rm L} + t)(V_{\rm in}t - i_{40}L) - n^2C_{\rm f}R_{\rm L}V'_{\rm o4}}{n^2C_{\rm f}R_{\rm L} + (nL - R_{\rm L}t)t} \end{cases} \tag{A3}$$

$$\begin{cases} V'_{\rm o5}(t) = \dfrac{LR_{\rm L}\left(n^2C_{\rm f}V'_{\rm o5} - i_{50}t\right)}{n^2C_{\rm f}R_{\rm L} + (nL + R_{\rm L}t)t} \\ i_5(t) = \dfrac{n(i_{50}Lt + nC_{\rm f}R_{\rm L}(i_{50}L + V'_{\rm o5}t))}{n^2C_{\rm f}R_{\rm L} + (nL + R_{\rm L}t)t} \end{cases} \tag{A4}$$

$$\begin{cases} V'_{\rm o6}(t) = \dfrac{LR_{\rm L}\left(n^2C_{\rm f}V'_{\rm o6} - i_{60}t\right)}{n^2C_{\rm f}R_{\rm L} + (nL - R_{\rm L}t)t} \\ i_6(t) = \dfrac{n(i_{60}Lt + nC_{\rm f}R_{\rm L}(i_{60}L - V'_{\rm o6}t))}{n^2C_{\rm f}R_{\rm L} + (nL - R_{\rm L}t)t}. \end{cases} \tag{A5}$$

REFERENCES

[1] Y. Li, X. Lyu, D. Cao, S. Jiang, and C. Nan, "A 98.55% efficiency switched-tank converter for data center application," *IEEE Trans. Ind. Appl.*, vol. 54, no. 6, pp. 6205–6222, Nov./Dec. 2018.
[2] D. Rothmund, T. Guillod, D. Bortis, and J. W. Kolar, "99% Efficient 10 kV SiC-based 7 kV/400 V DC transformer for future data centers," *IEEE J. Emerg. Sel. Topics Power Electron.*, vol. 7, no. 2, pp. 753–767, Jun. 2019.
[3] B. Yang, F. C. Lee, A. J. Zhang, and G. Huang, "LLC resonant converter for front end DC/DC conversion," in *Proc. IEEE APEC*, Mar. 2002, pp. 1108–1112.

[4] L. H. Mweene, C. A. Wright, and M. F. Schlecht, "A 1 kW, 500 kHz front-end converter for a distributed power supply system," *IEEE Trans. Power Electron.*, vol. 6, no. 3, pp. 398–407, Jul. 1991.
[5] M. Farhadi and O. Mohammed, "Energy storage technologies for high-power applications," *IEEE Trans. Ind. Appl.*, vol. 52, no. 3, pp. 1953–1961, May/Jun. 2016.
[6] Z. Xiao, Y. Jiang, T. Sun, Y. Wu, and Y. Tang, "Refining power converter loss evaluation: A transfer learning approach," *IEEE Trans. Power Electron.*, vol. 39, no. 4, pp. 4313–4324, Apr. 2024.
[7] Z. Liang, R. Guo, J. Li, and A. Q. Huang, "A high-efficiency PV module-integrated DC/DC converter for PV energy harvest in FREEDM systems," *IEEE Trans. Power Electron.*, vol. 26, no. 3, pp. 897–909, Mar. 2011.
[8] F. Lu, H. Zhang, H. Hofmann, and C. Mi, "A double-sided LCLC-compensated capacitive power transfer system for electric vehicle charging," *IEEE Trans. Power Electron.*, vol. 30, no. 11, pp. 6011–6014, Nov. 2015.
[9] X. Zhou et al., "A high-efficiency high-power-density on-board low-voltage DC–DC converter for electric vehicles application," *IEEE Trans. Power Electron.*, vol. 36, no. 11, pp. 12781–12794, Nov. 2021.
[10] 2015. 80 Plus. [Online]. Available: www.80plus.org
[11] 2015. Energy start. [Online]. Available: www.energystar.gov
[12] R. W. De Doncker, D. M. Divan, and M. H. Kheraluwala, "A three-phase soft-switched high power density DC/DC converter for high power applications," in *Proc. Conf. Rec. IEEE Ind. Appl. Soc. Annu. Meeting*, Oct. 1988, vol. 1, pp. 796–805.
[13] R. W. DeDoncker, D. M. Divan, and M. H. Kheraluwala, "A three-phase soft-switched high power density DC-to-DC converter for high power applications," *IEEE Trans. Ind. Appl.*, vol. 27, no. 1, pp. 63–73, Jan./Feb. 1991.
[14] B. Zhao, Q. Song, and W. H. Liu, "Efficiency characterization and optimization of isolated bidirectional DC–DC converter based on dual-phase-shift control for DC distribution application," *IEEE Trans. Power Electron.*, vol. 28, no. 4, pp. 1711–1727, Apr. 2013,.
[15] H. Bai and C. Mi, "Eliminate reactive power and increase system efficiency of isolated bidirectional dual-active-bridge DC–DC converters using novel dual-phase-shift control," *IEEE Trans. Power Electron.*, vol. 23, no. 6, pp. 2905–2914, Nov. 2008.
[16] B. Zhao, Q. G. Yu, and W. X. Sun, "Extended-phase-shift control of isolated bidirectional DC–DC converter for power distribution in micro-grid," *IEEE Trans. Power Electron.*, vol. 27, no. 11, pp. 4667–4680, Nov. 2012.
[17] H. Shi et al., "Minimum-backflow-power scheme of DAB-based solid-State transformer with extended-phase-shift control," *IEEE Trans. Ind. Appl.*, vol. 54, no. 4, pp. 3483–3496, Jul./Aug. 2018.
[18] Z. Xiao, Z. He, Z. Li, L. Zhu, and L. Wang, "Unified description and optimization method of Dual Active Bridge DC–DC converters," *IEEE Trans. Power Electron.*, vol. 37, no. 10, pp. 11839–11854, Oct. 2022.
[19] A. Tong, L. Hang, G. Li, X. Jiang, and S. Gao, "Modeling and analysis of a dual-active-bridge-isolated bidirectional DC/DC converter to minimize RMS current with whole operating range," *IEEE Trans. Power Electron.*, vol. 33, no. 6, pp. 5302–5316, Jun. 2018.
[20] F. Krismer and J. W. Kolar, "Closed form solution for minimum conduction loss modulation of DAB converters," *IEEE Trans. Power Electron.*, vol. 27, no. 1, pp. 174–188, Jan. 2012.
[21] W. Choi, K. Rho, and B. Cho, "Fundamental duty modulation of Dual-Active-bridge converter for wide-range operation," *IEEE Trans. Power Electron.*, vol. 31, no. 6, pp. 4048–4064, Jun. 2016.
[22] J. Everts, F. Krismer, J. Van den Keybus, J. Driesen, and J. W. Kolar, "Optimal ZVS modulation of single-phase single-stage bidirectional DAB AC–DC converters," *IEEE Trans. Power Electron.*, vol. 29, no. 8, pp. 3954–3970, Aug. 2014.
[23] G. G. Oggier and M. Ordonez, "High-efficiency DAB converter using switching sequences and burst mode," *IEEE Trans. Power Electron.*, vol. 31, no. 3, pp. 2069–2082, Mar. 2016.
[24] J. Hiltunen, V. Väisänen, R. Juntunen, and P. Silventoinen, "Variable-frequency phase shift modulation of a dual active bridge converter," *IEEE Trans. Power Electron.*, vol. 30, no. 12, pp. 7138–7148, Dec. 2015.
[25] J. Riedel, D. G. Holmes, B. P. McGrath, and C. Teixeira, "Maintaining continuous ZVS operation of a dual active bridge by reduced coupling transformers," *IEEE Trans. Ind. Electron.*, vol. 65, no. 12, pp. 9438–9448, Dec. 2018.
[26] Z. Qin, Y. Shen, P. C. Loh, H. Wang, and F. Blaabjerg, "A dual active bridge converter with an extended high-efficiency range by DC blocking capacitor voltage control," *IEEE Trans. Power Electron.*, vol. 33, no. 7, pp. 5949–5966, Jul. 2018.
[27] P. Liu and S. Duan, "A ZVS range enhancement strategy for the DAB converter by using blocking capacitors," *IEEE J. Emerg. Sel. Topics Power Electron.*, vol. 9, no. 2, pp. 1389–1398, Apr. 2021.
[28] Z. Xiao, Y. Jiang, F. Deng, Z. Yao, and Y. Tang, "A data-driven control parameters optimization method for dual active bridge converters," *IEEE Trans. Ind. Electron.*, vol. 71, no. 11, pp. 14054–14066, Nov. 2024.
[29] X. Li, X. Zhang, F. Lin, C. Sun, and K. Mao, "Artificial-intelligence-based triple phase shift modulation for dual active bridge converter with minimized current stress," *IEEE J. Emerg. Sel. Topics Power Electron.*, vol. 11, no. 4, pp. 4430–4441, Aug. 2023.
[30] Z. Xiao et al., "A hybrid data-driven power loss minimization method of dual-active bridge converters," *IEEE Trans. Power Electron.*, vol. 39, no. 5, pp. 5820–5832, May 2024.
[31] Texas Instruments, "UCC25600: 8-Pin high-performance resonant mode controller," Jul. 2015. [Online]. Available: https://www.ti.com.cn/product/zh-cn/UCC25600
[32] L. Zhang, R. Born, X. Zhao, B. Gu, J. -S. Lai, and H. Ma, "A parabolic voltage control strategy for burst-mode converters with constant burst frequency and eliminated audible noise," *IEEE Trans. Power Electron.*, vol. 31, no. 12, pp. 8572–8580, Dec. 2016.
[33] J. Chen, Y. Hwang, C. Jheng, Y. Ku, and C. Yu, "A low-electromagnetic-interference buck converter with continuous-time delta-sigma-modulation and burst-mode techniques," *IEEE Trans. Ind. Electron.*, vol. 65, no. 9, pp. 6860–6869, Sep. 2018.
[34] W. Feng, F. C. Lee, and P. Mattavelli, "Optimal trajectory control of burst mode for LLC resonant converter," *IEEE Trans. Power Electron.*, vol. 28, no. 1, pp. 457–466, Jan. 2013.
[35] Z. Xiao, X. Li, and Y. Tang, "A lightweight artificial neural network start-up controller for CLLC resonant converters," *IEEE Trans. Power Electron.*, vol. 39, no. 11, pp. 14775–14786, Nov. 2024.
[36] C. Fei, Q. Li, and F. C. Lee, "Digital implementation of light-load efficiency improvement for high-frequency LLC converters with simplified optimal trajectory control," *IEEE J. Emerg. Sel. Topics Power Electron.*, vol. 6, no. 4, pp. 1850–1859, Dec. 2018.
[37] H. Akagi, T. Yamagishi, N. M. L. Tan, S.-I. Kinouchi, Y. Miyazaki, and M. Koyama, "Power-loss breakdown of a 750-V 100-kW 20-kHz bidirectional isolated DC–DC converter using SiC-MOSFET/SBD dual modules," *IEEE Trans. Ind. Appl.*, vol. 51, no. 1, pp. 420–428, Jan./Feb. 2015.
[38] M. Kasper, R. M. Burkart, G. Deboy, and J. W. Kolar, "ZVS of power MOSFETs revisited," *IEEE Trans. Power Electron.*, vol. 31, no. 12, pp. 8063–8067, Dec. 2016.
[39] J. Muhlethaler, J. Biela, J. W. Kolar, and A. Ecklebe, "Improved core-loss calculation for magnetic components employed in power electronic systems," *IEEE Trans. Power Electron.*, vol. 27, no. 2, pp. 964–973, Feb. 2012.

Ziheng Xiao (Member, IEEE) received the B.S. degree in electrical engineering and automation and the Ph.D. degree in electrical engineering from the College of Electrical and Information Engineering, Hunan University, Changsha, China, in 2017 and 2022, respectively.

Since 2022, he has been a Research Fellow with Energy Research Institute, Nanyang Technological University, Singapore. His main research interests include the medium voltage dc system, dual active bridge converters, resonant converters, energy router in renewable energy systems, and the application of artificial intelligence in power electronics. Dr. Xiao was a recipient of the Best Paper Award First Prize in ECCE Asia in 2024. He was the Session chair for the 49th Annual Conference of the IEEE Industrial Electronics Society.

Muxuan Xiao was born in Hunan, China, in 1989. He received the B.S. degree in automation from Hubei University of Automotive Technology, Shiyan, China, in 2011, the M.S. degree and the Ph.D. degree in electrical engineering from Hunan University, Changsha, China, in 2014 and 2021.

Now he is doing postdoc research in electrical engineering from Hunan University. His research interests include dc/dc converter, motor driver and multilevel converter.

Zhixing He (Member, IEEE) was born in Hunan, China, in 1989. He received the B.S. degree in information science and Engineering from Central South University, Changsha, China, in 2011, and the Ph.D. degree in electrical engineering from Hunan University, Changsha, China, in 2017.

He was with the Hunan University, as Postdoctoral Researcher between 2017 and 2018. He has been an Associate Professor with the College of Electrical and Information Engineering, Hunan University, Changsha, China. His research interests include power electronics, medium voltage dc system, model predictive control, and modular multilevel converter.

Liang Wang was born in Hunan, China, in 1987. He received the M.S. degree in mechatronic engineering from the University of Shanghai for Science and Technology, Shanghai, China, in 2013. He is currently working toward the Ph.D. degree in electrical engineering with the College of Electrical and Information Engineering, Hunan University, Changsha, China.

His main research interests include power electronics, silicon carbide power electronic devices, and their applications in induction heat treatment applications.

Zongjian Li (Member, IEEE) received the B.S. degree in electronic information engineering from the College of engineering, Hunan Normal University, Changsha, China, in 2012, and the Ph.D. degree in electric engineering from Hunan University, Changsha, China, in 2020.

He is currently a Postdoctoral with the College of Electrical and Information Engineering, Hunan University, Changsha, China. His research interests include silicon carbide power electronic devices and their applications in high voltage converter applications. His current research interests include the medium voltage dc system, resonant dc converter, and CC/CV dc/dc converters.

Hongliang Wang (Senior Member, IEEE) received the B.Sc. degree in electrical engineering from Anhui University of Science and Technology, Huainan, China, in 2004, and the Ph.D. degree in electrical engineering from Huazhong University of Science and Technology, Wuhan, China, in 2011.

From 2004 to 2005, he was an Electrical Engineer with Zhejiang Hengdian Thermal Power Plant. From 2011 to 2013, he was a Senior System Engineer at Sungrow Power Supply Co. Ltd. From 2013–2018, he was a Postdoctoral Fellow with Queen's University. Since 2018, he has been with Hunan University, where he is currently a Full Professor with the College of Electrical and Information Engineering. He has authored more than 60 technical papers in the Journals and conferences. He is the inventor/coinventor of 42 China issued patents, 8 US issued patents. His current research interests include multilevel topology, high-gain topology, parallel technology, and virtual synchronous generator technology for photovoltaic application and microgrids application; resonant converters and server power supplies, and LED drivers.

Dr. Wang is currently a senior member of China Electro-Technical Society, a senior member of China Power Supply Society (CPSS). He is a member of CPSS Technical Committee on Standardization; a member of CPSS Technical Committee on Renewable Energy Power Conversion, a China Expert Group Member of IEC Standard TC8/PT 62786, a Vice-Chair of IEEE Kingston Section, a Session Chair of ECCE 2015 and ECCE2017, and a TPC member of ICEMS2012.